Highlights

Wave-Ice Interaction for Regional Applications: SWAN Developments and Validations

Nirnimesh Kumar, W. Erick Rogers, Jim Thomson, Clarence Collins

- SWAN wave model, extended to account for effects of sea ice, is applied for the first time
- Modeled spectral energy density and significant wave height reasonably agree in the Barents Sea and the Gulf of Bothnia
- Cumulative fetch laws are validated using modeled wave energy in marginal ice zone

Wave-Ice Interaction for Regional Applications: SWAN Developments and Validations

Nirnimesh Kumar[a,*], W. Erick Rogers[b,**], Jim Thomson[c], Clarence Collins[d]

[a]*Department of Civil & Environmental Engineering, University of Washington, Seattle WA*
[b]*Naval Research Laboratory, Stennis Space Center, Mississippi*
[c]*Applied Physics Laboratory, University of Washington, Seattle, WA*
[d]*Field Research Facility, United States Army Corps of Engineers*

Abstract

Interaction between surface gravity waves and sea-ice in the marginal ice zone is complex. Most of the prior research focus in this subject has been in deeper oceans. Here, the regional wave model Simulating WAves Nearshore (SWAN) is configured to simulate wave dissipation and reduced wind-generation in the presence of sea-ice. Wind-generation is modified by scaling the generation terms with the open-water fraction, while wave dissipation due to sea-ice is simulated as an exponential energy decay as function of ice concentration and wave frequency. This sea-ice induced dissipation is preferentially at higher frequencies with implications for reduction in sea-surface roughness and Stokes drift shear. Modified SWAN is validated for interaction between regional sea-ice and a storm event in the Barents Sea, and in the Gulf of Bothnia. In the Barents sea, SWAN simulation with wave-ice interaction reasonably agrees with measured wave parameters. In the shallow seas of Gulf of Bothnia, modeled wave dynamics agrees well with satellite altimetry based significant wave height. This model setup is used to understand fetch scaling in the marginal ice zone. The non-dimensional energy scales well with a non-dimensional fetch determined from a cumulative fetch dependent on ice concentration. Implications for Stokes drift in the marginal ice zone are also discussed for the Bothnian Bay. Finally, recommendations for parameterization of dependency of wave dissipation to ice thickness are discussed.

Keywords: Wave-ice Interaction, Fetch Scaling, Stokes drift, Barents Sea, Gulf of Bothnia

1. Introduction

Surface gravity waves are one of the most common features at the air-water interface, with implications for exchange of heat, gases, momentum and energy (*e.g.,* Steele et al., 1989; Agrawal et al., 1992; Melville, 1996). Wave-induced mass flux (*i.e.,* Stokes drift, u^{St})

*Deceased 30 August 2020
**Corresponding author
Email address: erick.rogers@nrlssc.navy.mil (W. Erick Rogers)

modifies the Lagrangian transport and interacts with the mean velocity shear to generate Langmuir circulation cells and upper-ocean mixing through Langmuir turbulence (Tejada-Martinez and Grosch, 2007; D'Asaro, 2014). In coastal waters, surface gravity waves modify coastal ocean circulation and vertical mixing. Wave-breaking driven cross-shore and alongshore circulation, rip currents and eddies (Dalrymple et al., 2011) transport tracers (*e.g.,* pollutants, larvae) to deeper waters.

At higher latitudes and in the polar ocean, presence of sea-ice in the ocean modifies propagation and transformation of surface waves in the marginal ice zone (hereinafter MIZ), a region between the open ocean and pack ice. Interaction between sea-ice and surface waves (hereinafter, wave-ice interaction) in the MIZ has been observed through field measurement campaigns (*e.g.,* Wadhams et al., 1986; Doble and Bidlot, 2013; Kohout et al., 2014; Thomson and Rogers, 2014; Gemmrich et al., 2018; Thomson et al., 2018), however, this interaction is still an active area of research with primary focus in the deeper ocean. Presence of sea-ice in the coastal ocean, or MIZs in the coastal shelf may change the surface waves properties reaching the coastal waters, and therefore modify the aforementioned wave-driven processes.

Multiple theoretical models represent the interaction between surface waves and sea-ice of different ice types (*e.g.,* Squire et al., 1995; Squire, 2007, 2020). For sparsely spread ice floes, wave-ice interaction is modeled through exponential wave-attenuation determined as a function of water depth, floe diameter and thickness (*e.g.,* Wadhams et al., 1988; Kohout and Meylan, 2008). For compact and potentially colliding ice floes, mathematical models treat ice floes as a single viscous fluid layer with specific rheology (*e.g.,* Weber, 1987; Keller, 1998). Such models require eddy viscosity and density for the ice-water layer, and are applied to study grease ice (Newyear and Martin, 1999). Complex two-layer viscoelastic theoretical models provide a unified rheology for ice layer treated as a viscous fluid layer by considering the elasticity quantified through the shear modulus (Wang and Shen, 2010). For highly compact ice (*e.g.,* shorefast ice), multiple studies attribute wave dissipation due to turbulence in the boundary layer beneath the ice layer (*e.g.,* Liu and Mollo-Christensen, 1988; Liu et al., 1991, 1994; Ardhuin et al., 2018).

Application of the aforementioned wave-ice interaction theories is potentially challenging for operational wave modeling in the MIZ, as some of the assumptions in theoretical model derivations may not always be valid in field. Also, some of the input variables required might not be readily available, or might be of poor fidelity (*e.g.,* ice type). Historically, an empirical grid obstruction approach based on ice concentration has existed in the operational operational wave model WAVEWATCH III (WW3, Tolman, 2003; Tolman and The WAVEWATCH III ® Development Group, 2014), which is often referred to as the IC0 method. The third generation model WAM also uses the grid obstruction method (Tolman, 2003) for ice concentration up to 70%, and has been applied to study wave-ice interaction in the Baltic Sea (Tuomi et al., 2019). Recently, substantial progress has been made in the adaptation of WW3 to include wave-ice interactions (Rogers and Orzech, 2013; Rogers et al., 2016). WW3 updated for surface wave-ice interaction provides multiple approaches for sea-ice induced wave-dissipation, which include,

1. Exponential wave energy decay as a function of ice coverage (IC1)

2. Wave-dissipation due to turbulence at ice-water interface (IC2, Liu et al., 1991; Rogers and Orzech, 2013; Stopa et al., 2016)
3. Wave-dissipation through interaction with an ice continuum model which treats ice as a viscoelastic layer (IC3, Wang and Shen, 2010)
4. Exponential wave energy decay as a function of ice concentration and wave frequency, as established from empirical fits to field measurements (IC4, Meylan et al., 2014; Collins and Rogers, 2017; Rogers et al., 2018).
5. Ice-induced wave decay based on introducing viscosity into the thin elastic plate model of Fox and Squire (1994) (IC5, Mosig et al., 2015)

The modified WW3 is validated against wave measurements in the Beaufort and Chukchi Seas (*e.g.,* Thomson and Rogers, 2014; Thomson et al., 2016; Rogers et al., 2016; Collins and Rogers, 2017; Gemmrich et al., 2018). Furthermore, these recent approaches (*e.g.,* IC4) have been more successful in simulating wave dynamics in the marginal ice zone as compared to the historical grid obstruction approach, IC0 (Fig. 11 Thomson et al., 2018). The progress in WW3 is primarily intended for deep water applications and global domains. In addition to dissipation through interaction with ice, wave scattering occurs as well. Recent studies have simulated wave scattering due to ice in the Arctic (*e.g.,* Ardhuin et al., 2016) and relevant formulations have been discussed in section 2.

Even though WW3 provides a versatile operational tool for wave-ice interaction, its use in high-resolution wave modeling and coastal regions is limited. Conversely, Simulating WAves Nearshore (SWAN) is a widely used model for coastal applications with the primary literature (Booij et al., 1999) having received 4274 citations[1]. For example, the U.S. Navy still uses SWAN for much of its high-resolution regional wave modeling, for reasons of efficiency and relative ease of use. These operational models include regions that are seasonally ice-infested, such as the Baltic Sea and the Gulf of Bothnia. Yet, there was no representation of sea ice in prior versions (*i.e.,* v41.20) of SWAN (still used operationally at time of writing), which can substantially reduce model accuracy in coastal regions at higher latitudes (Rogers, 2019). Like WW3, SWAN is governed by similar set of equations; however, WW3 primarily uses an explicit time-stepping scheme[2] and is more efficient at larger scales, while SWAN uses implicit time stepping and is better for regional and coastal scales (Rogers et al., 2007). The grid obstruction approach, ICO historically available in WW3 (Tolman, 2003), was also not available in SWAN. Previous efforts to include the role of ice in SWAN simulations include: (1) running SWAN in open water to provide incident wave conditions for use in simple, external calculations of wave transmission and losses, or (2) deactivating ice-covered grid points in SWAN by changing them to land points (*e.g.,* Hoque et al., 2019).

Here, the focus of this paper is to discuss the development and application of SWAN for wave-ice interaction. Weighing the relative strengths of the approaches used in WW3 (*i.e.,* IC1-IC5), dissipation of wave energy by sea-ice is incorporated in SWAN only using

[1]Retrieved from Google Scholar, July 6 2020.

[2]WW3 developments focused on implicit time stepping and unstructured grid are underway (*e.g.,* Roland and Ardhuin, 2014), however, these updates have not been integrated yet for U.S. Navy operational wave modeling

the IC4+Method 2 or IC4M2 methodology, *i.e.,* a simple empirical parametric model (polynomial function) for dissipation by sea ice following previous efforts (Meylan et al., 2014; Collins and Rogers, 2017; Rogers et al., 2018). Effectively, this also permits use of IC1 in SWAN, since IC1 can be recovered using particular settings with IC4M2. This new SWAN code has been validated for idealized and analytical test cases (Rogers, 2019). Here, these latest developments in the SWAN code are tested for realistic applications in the Barents Sea and the Gulf of Bothnia. SWAN simulated dynamics in the MIZ and shallow seas provides an opportunity to understand the implications for other wave-driven oceanographic processes, which have not been extensively considered in previous studies. Modeled wave bulk and spectral parameters are compared to observations, while fetch scalings for the MIZ, and implications for Stokes drift are discussed. Finally, recommendations for inclusion of dependency of wave dissipation to ice thickness is also considered.

The equations for model setup and updates are in section 2. The model application for the Barents Sea and the Gulf of Bothnia are presented in section 3. Discussions related to fetch scalings, Stokes drift and future recommendations are considered in section 4, followed by a summary in section 5. Access to updated code and data dissemination is in the Acknowledgement section.

2. SWAN Model Development

The third generation, spectral SWAN wave model (Booij et al., 1999; Ris et al., 1999) solves the action-balance equation, and simulates shoaling, wave refraction due to both bathymetry and mean currents, energy input due to winds, energy loss due to white-capping, bottom friction, and depth-limited breaking.

2.1. Action-Balance Equation

The wave action spectral density N (hereinafter action density), defined as the ratio of wave energy spectral density, E and the relative frequency σ is a conservative quantity in the presence of ambient mean flows (Bretherton and Garrett, 1968), and a function of the relative wave frequency σ, direction θ, space (x, y) and time (t), such that $N = N(\sigma, \theta, x, y, t)$. The rate of change of action density at a point is determined from the action-balance equation (Mei, 1989; Komen et al., 1996):

$$\frac{\partial N}{\partial t} + \nabla_{\vec{x}} \cdot [(\vec{c}_g + \vec{U})N] + \frac{\partial c_\sigma N}{\partial \sigma} + \frac{\partial c_\theta N}{\partial \theta} = \frac{S_{\text{tot}}}{\sigma}, \tag{1}$$

where $\vec{c}_g = \partial\sigma/\partial\vec{k}$ is the group velocity, $\vec{U}$ is the ambient mean flow, and c_σ, c_θ are propagation velocities in the spectral space. The first term on the left (Eq. 1) is the rate of change of action density, while the second term represents energy propagation in the geographic space including the effect of wave shoaling. The effect of shifting in mean frequency due to changing depth and mean currents is represented by the third left hand side term, and the fourth term represents depth and current-induced refraction (Booij et al., 1999). The relative wave frequency is related to the wave number through the dispersion relation such

that $\sigma^2 = g|\vec{k}| \tanh |\vec{k}|h$, where $\vec{k}$ is the wavenumber vector, h is the water depth, and $|\ |$ represents an absolute value. The right hand side of Eq. 1 contains non-conservative source and sink terms such that

$$S_{\text{tot}} = S_{\text{in}} + S_{\text{nl3}} + S_{\text{nl4}} + S_{\text{ds,w}} + S_{\text{ds,b}} + S_{\text{ds,br}}, \tag{2}$$

where S_{in} is the source term indicative of wave growth due to wind input, S_{nl3} and S_{nl4} are nonlinear wave energy transfer from three and four wave interactions, and $S_{\text{ds,w}}$,$S_{\text{ds,b}}$, and $S_{\text{ds,br}}$ are wave dissipation due to whitecapping, bottom friction and depth-limited breaking, respectively. These terms in their present form do not include any wave-ice interaction.

2.2. Wave-dissipation due to Sea-Ice

The primary role of sea-ice is direct wave-dissipation and reduction of wave growth due to winds in the presence of partial ice-coverage. Both these effects modify the right-hand-side of the action-balance equation (Eq. 2), and the relevant input parameter is ice concentration denoted by a_{ice}.

Previous efforts in simulating wave-dissipation in presence of sea-ice (Collins and Rogers, 2017; Rogers et al., 2018) have successfully used the IC4 approach which assumes that wave energy decays exponentially in space, with the decay rate being a function of the wave frequency (Meylan et al., 2014). This decay is a sink term in the action-balance equation denoted by S_{ice} and is related to the exponential decay rate of energy (D_{ice}) as (Rogers and Orzech, 2013):

$$D_{\text{ice}} = \frac{S_{\text{ice}}}{E} = -2c_g k_i, \tag{3}$$

where k_i is the linear exponential decay rate of wave amplitude in geographical space. The factor of 2 in Eq. 3 converts amplitude decay to an energy decay, while the group velocity provides a conversion from spatial to temporal decay (*i.e.,* $\partial N/\partial s = (\partial N/\partial t)(\partial s/\partial t) = c_g(\partial N/\partial t)$). Both wave energy spectral density E and S_{ice} are function of wave frequency f and direction θ. However, energy decay rate D_{ice} and k_i are only a function of the wave frequency. The linear exponential decay rate of IC4M2 in SWAN is a polynomial of order 6 such that,

$$k_i = C_0 f^0 + C_1 f^1 + C_2 f^2 + C_3 f^3 + C_4 f^4 + C_5 f^5 + C_6 f^6, \tag{4}$$

where $C_0, C_1, C_2, \cdots$ are user-defined dimensional constants such that the unit of k_i is 1/m. These dimensional constants can be tuned to match observations, yet some guidelines for ice types are provided. For ice floes with a diameter of 10-25 m, $C_2 = 1.06 \times 10^{-3}$ and $C_4 = 2.30 \times 10^{-2}$ are suggested (Meylan et al., 2014), while for pancake and frazil ice, $C_2 = 0.284 \times 10^{-3}$ and $C_4 = 1.53 \times 10^{-2}$ (Rogers et al., 2018). The relative importance of dissipation due to presence of sea-ice is a function of the ice concentration, such that the ice sink function is expressed as:

$$S_{\text{ice,}_1} = a_{\text{ice}} S_{\text{ice}}, \tag{5}$$

where, $S_{\text{ice,}_1}$ is the value after scaling due to the ice concentration.

2.3. Scaling of Wind-Induced Wave Growth

One of the other implications of sea-ice presence is reduction in the growth rate of wind waves. Even though this is an active area of research (Smith and Thomson, 2016; Gemmrich et al., 2018), presently the simplest approach is utilized, *i.e.,* scaling of the wind-input term with the open-water fraction. The variable Ω_{iw} controls the wind-input scaling in the SWAN code, with a default value of $\Omega_{iw} = 0$ indicating scaling of wave growth from open-water fraction. The scaling factor (F_{in}) is given as:

$$F_{\text{in}} = (1 - a_{\text{ice}}(1 - \Omega_{iw})), \tag{6a}$$

or

$$F_{\text{in}} = a_{\text{water}} + a_{\text{ice}}\Omega_{iw}, \tag{6b}$$

such that

$$a_{\text{water}} + a_{\text{ice}} = 1. \tag{6c}$$

By accounting for reduced wave growth and wave dissipation in the presence of sea-ice the new action balance equation in SWAN is:

$$\begin{aligned}\frac{\partial N}{\partial t} + \nabla_{\vec{x}} \cdot [(\vec{c}_g + \vec{U})N] + \frac{\partial c_\sigma N}{\partial \sigma} + \frac{\partial c_\theta N}{\partial \theta} = \frac{1}{\sigma}\left\{F_{\text{in}} S_{\text{in}} + S_{\text{nl3}} + S_{\text{nl4}}\right\} \\ + \frac{1}{\sigma}\left\{S_{\text{ds,w}} + S_{\text{ds,b}} + S_{\text{ds,br}} + a_{\text{ice}} S_{\text{ice}}\right\},\end{aligned} \tag{7}$$

which for a default scaling of $\Omega_{iw} = 0$ reduces to:

$$\begin{aligned}\frac{\partial N}{\partial t} + \nabla_{\vec{x}} \cdot [(\vec{c}_g + \vec{U})N] + \frac{\partial c_\sigma N}{\partial \sigma} + \frac{\partial c_\theta N}{\partial \theta} = \frac{1}{\sigma}\left\{a_{\text{water}} S_{\text{in}} + S_{\text{nl3}} + S_{\text{nl4}}\right\} \\ + \frac{1}{\sigma}\left\{S_{\text{ds,w}} + S_{\text{ds,b}} + S_{\text{ds,br}} + a_{\text{ice}} S_{\text{ice}}\right\}.\end{aligned} \tag{8}$$

2.4. Wave-scattering due to Sea-Ice

Wave scattering due to ice in the Arctic is also important and scattering-based parameterizations (*e.g.,* Ardhuin et al., 2016, amongst others) are also used for wave attenuation in recent studies focusing on wave-ice interactions (*e.g.,* Roach et al., 2018; Bateson et al., 2019; Zhang et al., 2020). In WW3, sea-ice induced scattering is considered as:

1. Scattering with fraction of wave energy being scattered proportional to the sea-ice concentration (IS1, Tolman and The WAVEWATCH III® Development Group, 2014).
2. Linear Boltzmann equation to model wave scattering in the MIZ (Meylan and Masson, 2006) with ice breakup and creep-based dissipation (IS2, Boutin et al., 2018).

These methods for incorporating wave scattering due to sea-ice is not implemented in the present study. Instead, the empirical dissipation term as parameterized in the IC4M2 algorithm encompasses the effects of all wave attenuation processes, including the role of scattering. Nonetheless, wave scattering also leads to directional energy redistribution, which

is not considered here. With limited observations of wave dissipation, scattering and subsequent energy redistribution, we see the present implementation as a practical approach for community usage.

2.5. Code Organization/Options in SWAN

The latest developments made as a part of this study have already been integrated with the official, publicly distributed SWAN code (v41.31, `http://swanmodel.sourceforge.net/download/download.htm`). Development version of this code (v41.20ABi) is maintained as a separate svn repository by Kumar, with access available for further development. The SWAN development release (v41.20ABi) was evaluated for a variety of idealized test cases, available to be checked out from the development repository. Further details are provided in the publicly available report (Rogers, 2019).

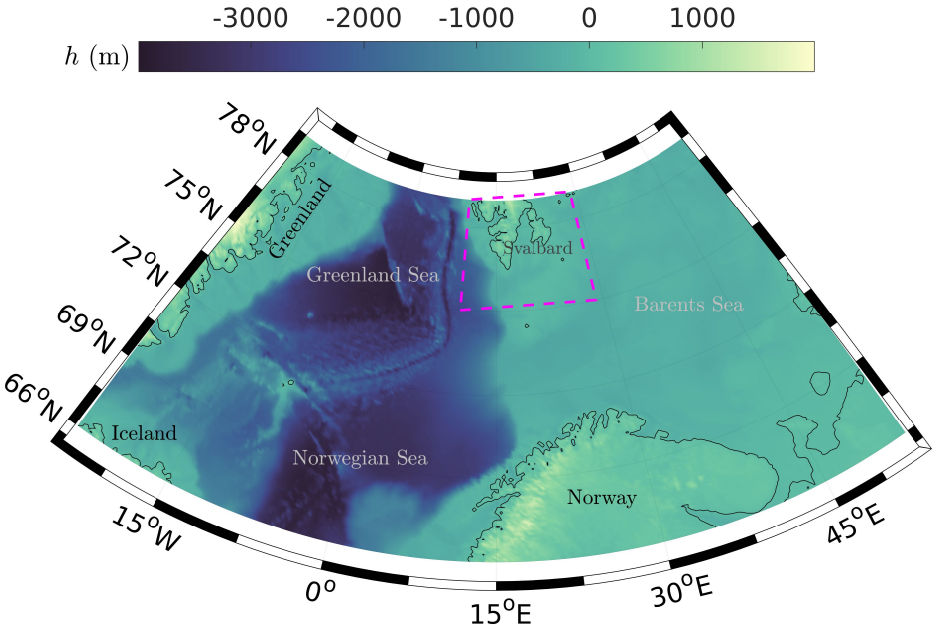

Figure 1: SWAN grid for the Barents Sea study region with a mean grid resolution of 3.24 km. Colorbar is the water depth h in meters. Surrounding geographical regions, Greenland, Iceland, Norway are also annotated. The magenta box outlines the region with ice coverage discussed in Figure. 2.

3. Model Evaluation for Realistic Configurations

The focus of this study is to evaluate the latest SWAN wave-ice interaction implementation for realistic applications. In particular, two applications are considered here for the Barents Sea and Gulf of Bothnia.

3.1. Barents Sea

The R/V *Lance* encountered an energetic wave event in the Barents Sea on May 2, 2010 (Fig. 1). Onboard Global Positioning System (GPS) on the vessel measured location

and vertical position at a sampling frequency of 1 Hz, with an accuracy of approximately 0.05 m. The vessel was treated as a surface following wave buoy acting as a low-pass filter to the ambient surface wave field (Collins III et al., 2015). The highest frequency response registered by the vessel is $f = 0.249$ Hz for waves approaching the vessel broadside. Wave measurements from a moving vessel lead to additional challenges in interpretation due to Doppler shift, which modifies the dispersion relationship. Even though algorithms exist to correct these effects (Collins III et al., 2017), we use an approach consistent with previous studies based on using this dataset, such that all analysis is confined to periods when ship speed is below 3 ms^{-1}, which is at the most 10% of the wave phase speed (Collins III et al., 2015). Also, considering that vessels have dynamic stability when moving (*e.g.,* Thomson et al., 2015), a conservative approach is used such that highest frequency of comparison is limited to 0.20 Hz. With these constraints on frequency limits, two metrics are quantified,

$$H_s = 4\sqrt{\int_{f_{\min}}^{f_{\max}} E(f)df}, \tag{9a}$$

and

$$mss_{LP} = \int_{f_{\min}}^{f_{\max}} \frac{(2\pi f)^4 E(f)}{g^2} df, \tag{9b}$$

where H_s is the significant wave height, mss_{LP} is the low-pass filtered mean square slope (*e.g.,* Chen et al., 2016), $E(f)$ is the spectral energy density, $f_{\min} = 0.04$ Hz and $f_{\max} = 0.20$ Hz. The significant wave height is a prognostic quantity extensively used to define the general wave climatology for a region, and also a useful quantity for coastal management purposes. The mean square slope is dynamically related to the sea-surface roughness, and identifies the contribution of high frequency signal, especially, assuming a universal f^{-4} dependency (*e.g.,* Toba, 1973; Phillips, 1985).

3.1.1. SWAN Model Setup

SWAN updated for wave-ice interactions is setup to simulate realistic wave conditions in the Barents Sea. The model grid consists of a single domain with a mean resolution of 3.25 km, and covers a study region which includes most of the Barents Sea, and parts of the Greenland and the Norwegian Sea (Fig. 1). The model bathymetry is derived from ETOPO2 dataset (Center, 2006). Wind forcing every three hours is obtained from the U.S. Navy's contemporary operational analyses (*i.e.,* Navy Operational Global Atmospheric Prediction System, NOGAPS, Hogan and Rosmond, 1991). Sea-ice concentration is provided using AMSR-E Unified Level-3 product available daily at a resolution of 12.5 km (*e.g.,* Fig. 2).

The SWAN model is setup to run in third generation mode for wind input and whitecapping following algorithms based on Rogers et al. (2012). Swell dissipation (Ardhuin et al., 2010) and quadruplet interaction are considered, however, triad interaction and wave dissipation due to depth-limited breaking and bottom friction are not accounted for, and are not expected to change the primary order dynamics discussed here. The SWAN wave action balance equation is solved in frequency and directional space with 48 frequencies between 0.04 and 1 Hz, and 100 directional bands with a directional resolution of 3.6°. Any wave

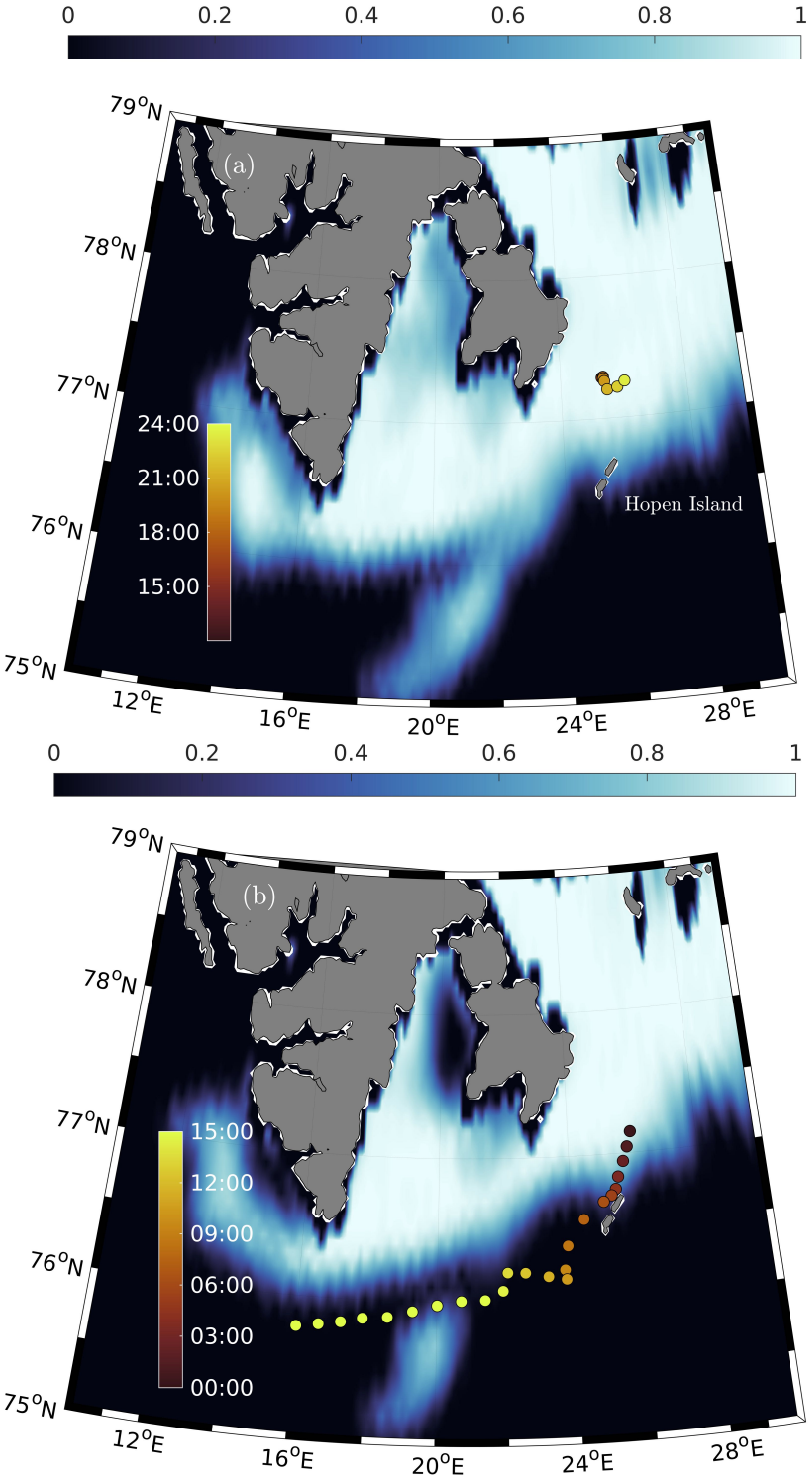

Figure 2: AMSR-E sea-ice concentration a_{ice} over parts of Barents and Norwegian sea on May 02, 2010 (a) and May 03, 2010 (b). The filled circles are R/V *Lance* tracks, with the color denoting time of the day in hours. The region shown here corresponds to the magenta box in Fig. 1.

activity within the study region is due to wind forcing including storm systems generated within the study domain, and no other wave forcing is provided at the open boundaries. Simulations are conducted without (hereinafter R_{NI}) and with wave-ice interactions (R_I) for a period of 20 days from April 20 to May 10, 2010. For the simulation with wave-ice interaction, wave dissipation due to the presence of ice is applied with the setting appropriate for ice floes with a diameter of 10-25 m (*i.e.,* $C_2 = 1.06 \times 10^{-3}$ and $C_4 = 2.30 \times 10^{-2}$), and wind-input is scaled with the open-water fraction ($\Omega_{iw} = 0$).

3.1.2. Ice Concentration and Ship Track

Wave measurements from R/V *Lance* are available from May 01-03, 2010. However, from the previously discussed data reduction constraints (section 3.1), measurements only for a 21 hour period from May 02, 15:00 to May 03, 12:00 are considered. All times are in UTC. A low-pressure system over Northern Europe moved northeast on May 01, followed by strengthening over the Barents Sea. Energetic waves from this storm system were observed in the study region and encountered by R/V *Lance*.

On May 02, 2010 the vessel was located southeast of Svalbard, and about 75 km north/ northeast of the Hopen Island (Fig. 2a). Visual and shipboard imagery indicated continuous pack ice with flat surface covered with snow, and ice thickness of 0.5-0.6 m (Collins III et al., 2015). The AMSR-E imagery based sea-ice concentration, a_{ice} was ≥ 0.8 at most locations in southern Svalbard and around the Hopen Island. A tongue of relatively high sea-ice concentration (0.4-0.8) extended southwest from the Hopen island. Continued fracturing of sea-ice occurred on May 02, hypothesized to be caused by flexural-gravity waves. As the vessel traversed farther east (Fig. 2a), the ice cover changed from pack ice to broken floes (Collins III et al., 2015).

On May 03, 2010 the vessel steamed through the MIZ with a typical floe size of 5-10 m. High wave activity was measured during this period by waves generated from the aforementioned storm system. The vessel continued south/southwestward heading through the relatively protected waters in the shadow of Hopen Island (Fig. 2c), and again encountered large waves on exiting the swell shadow around 08:00 hours as it steamed onward south (Collins III et al., 2015). The AMSR-E imagery suggested that the ice edge recedes farther north on May 03 (Fig. 2c) and presence of a MIZ north/northwest of Hopen Island. The preexisting tongue of ice located southwest of the Hopen Island detached from the main ice pack.

3.1.3. Spatial Variability of Significant Wave Height

Previous SWAN simulations for the study region (Collins III et al., 2015), did not include the effects of wave-ice interaction. Here, the SWAN simulation with wave-ice interaction, R_I is used to determine the role of sea-ice in changing modeled wave dynamics. Snapshot of significant wave height H_s evolution at two instances, 05/02, 16:00 (Fig. 3a) and 05/03, 02:00 (Fig. 3b) are considered.

Storm system generated waves in the southeastern region of the Barents Sea propagate northwest into the MIZ (Fig. 3a). The sea-ice concentration varies from 0.25 (light gray, Fig. 3a) to 0.75 (solid black, Fig. 3a) over a length scale of approximately 30 km. In this

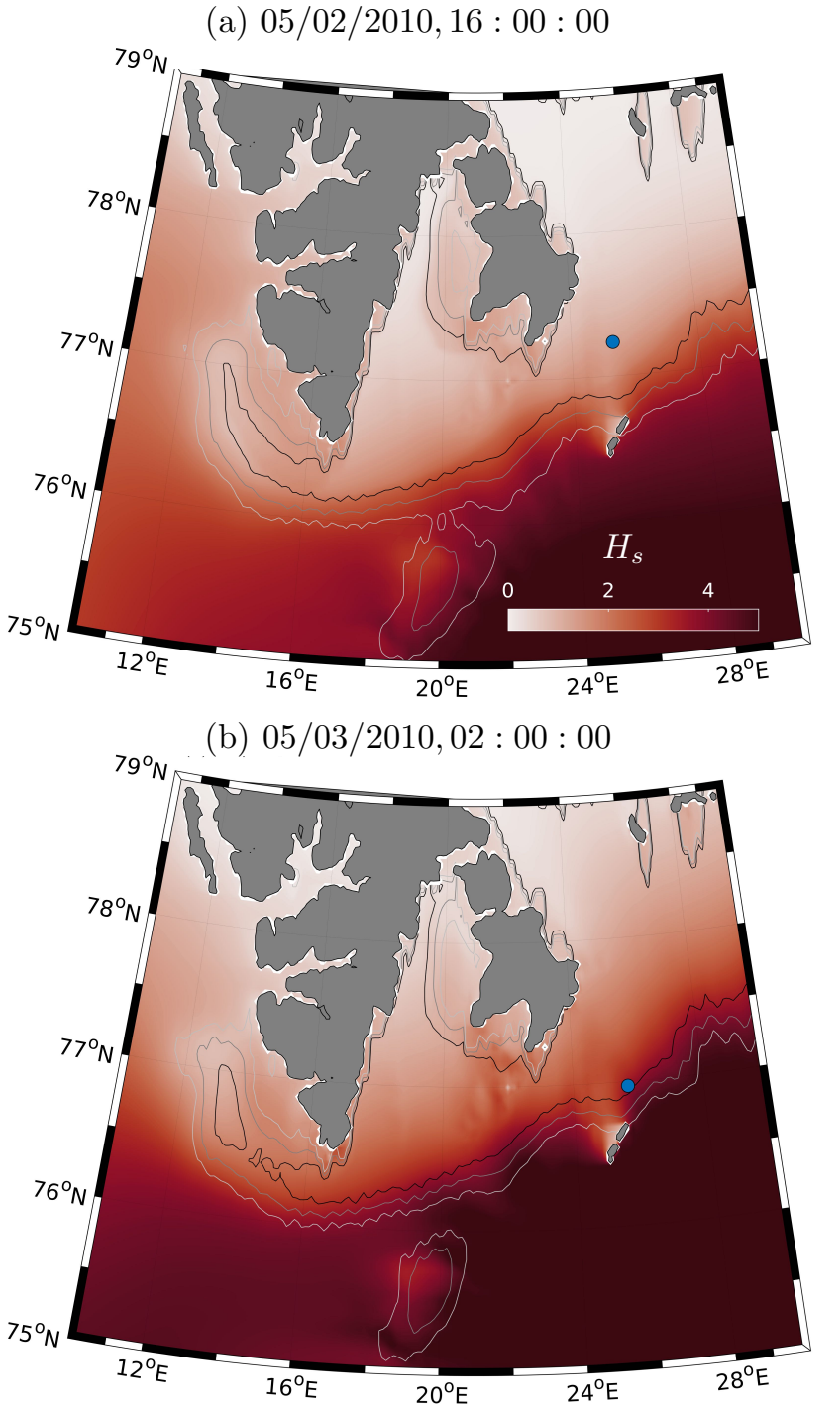

Figure 3: Color shading showing significant wave height H_s in the Barents Sea region for simulations with wave-ice interaction, R_I at times, (a) 05/02, 16:00:00; and (b) 05/03, 02:00:00. The position of R/V *Lance* is shown as the filled blue circle. Light gray, dark gray and black lines are contour lines representing sea-ice concentration $a_{\text{ice}} = 0.25$, 0.50 and 0.75, respectively. The region shown here corresponds to the magenta box in Fig. 1.

region, wave energy dissipates and the significant wave height H_s changes from 3 m to 1 m. Most of the region within 50 km from Svalbard has $H_s < 1$ m. As the storm system further intensifies, significant wave height in the southeastern Barents Sea and in the MIZ around Hopen Island increases. At the edge of the MIZ with sea-ice concentration $a_{\text{ice}} = 0.25$, significant wave height exceeds 5 m, decreasing to a magnitude of 2-3 m at regional locations with $a_{\text{ice}} = 0.75$ (solid black, Fig. 3b).

The sea-ice concentration also evolves as the MIZ recedes northwest (compare contour lines in Fig. 3a,b). Subsequently, waves generated from the storm event propagate farther northwest into the MIZ with $H_s > 2.5$ m around Svalbard (Fig. 3b). Even at locations with $a_{\text{ice}} = 0.5$, the $H_s > 4.0$ m. For these northwest propagating waves, Hopen Island creates a shadow zone with $H_s < 1$ m (Fig. 3b).

3.1.4. Obs. versus Modeled Wave Parameters

SWAN simulated significant wave height H_s and the mean square slope, mss_{LP} without, R_{NI} (blue, Fig. 4) and with, R_{I} (red, Fig. 4) wave-ice interaction are compared to observations from R/V *Lance*. Following Collins III et al. (2015) the 21 hour period is divided into five sub-periods corresponding to wave blocking by solid ice (15:00-20:00 hours, May 02, Red), ice breakup (20:00-21:00, May 02, Yellow), continued ice fracturing and interaction with swell event (21:00, May 02 to 03:00, May 03, Green), swell shadow (May 03, 03:00-08:00 hours, Cyan), and finally direct interaction with swell (May 03, 08:00-12:00 hours, Blue).

During the blocking period (red rectangle, Fig. 4) observed H_s is less than 25 cm. SWAN simulated H_s for R_{NI} (solid blue, Fig. 4a) varies from 3-4 m, and even for the simulation conducted with wave-ice interaction, R_{I} (solid red, Fig. 4a) H_s is over-estimated and is approximately 1.25-2.0 m. The observed mss_{LP} is negligible during the blocking period, which is captured by the simulation R_{I} (compare red and black squares, Fig. 4b). In this period even though the AMSR-E suggests an ice concentration, $a_{\text{ice}} = 1$ and the vessel was in pack ice, modeled wave dynamics indicate wave activity. This over-prediction of wave energy may occur if AMSR-E regional ice concentration in the MIZ southeastward from the measurement location is underestimated. Further, dissipation of waves may also depend on ice thickness. Measurements corresponding to this time indicates ice thickness greater than 0.5 m. However, ice thickness is not yet a parameter used in the SWAN wave-ice interaction model, therefore any dependency of wave dissipation to ice thickness is not yet accounted for SWAN.

Measured H_s rapidly increases from 0.25 to 3 m over the breakup period leading onto the swell event (yellow region, Fig. 4). SWAN simulated H_s accounting for wave-ice interaction does capture this transition, however the change is gradual than observed. Over the duration of the swell event (green region, Fig. 4) wave height increases from 3 to 4.5 m. The simulation R_{NI} over-estimates the wave height, while with wave-ice interaction H_s is underestimated in this period (compare red and blue squares to black squares, Fig. 4a). Mean square slope for the simulation R_{I} agrees well with observations during the breakup and the swell event.

As the vessel moves to the shadow region behind Hopen Island (Fig. 2c), the wave height decreases from 4.5 to 2 m, a trend captured by the simulations R_{NI} and R_{I}. However, the simulation with wave-ice interaction agrees slightly better (Fig. 4a). This good agreement is

also seen in comparison of mean square slope (Fig. 4b). In the latter half of the swell shadow event and during direct exposure to the storm-generated waves (cyan and blue region, Fig. 4) the model results from simulations R_{NI} and R_I are similar. This trend is expected with a lack of sea-ice at the vessel location (Fig. 2b). Caution must be exercised in any direct comparison for times later than May 03, 06:30, as the ship speed often exceeds 3 ms^{-1}.

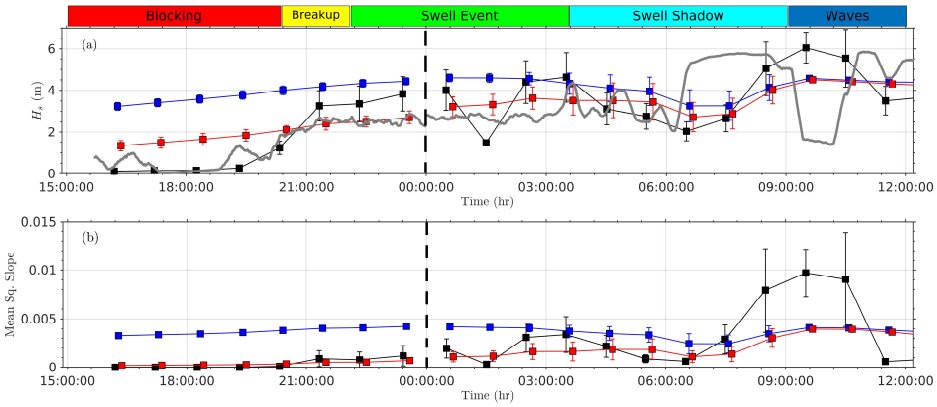

Figure 4: Observed (solid black) and modeled significant wave height H_s (a) and mean square slope, mss_{LP} (b) versus time. Model results w/o (blue, R_{NI}) and with ice (red, R_I) are shown. The shaded red, yellow, green, cyan and blue regions correspond to blocking, breakup, swell event, swell shadow, and exposure to waves, respectively. The gray line (a) is the ship speed in ms^{-1}. Standard deviation in observed H_s and mss_{LP} are from 95% confidence intervals to the estimated $E(f)$. Modeled standard deviation is from variability in modeled $E(f)$ estimates over a radius of 25 km from the location closest to the observation location.

3.1.5. Implications for Sea-surface elevation Spectra

Multiple previous studies have pointed at dissipation of high frequency waves propagating through the MIZ (*e.g.,* Meylan et al., 2014; Collins III et al., 2015; Rogers et al., 2016). Wave dissipation in sea-ice has been empirically formulated as an exponential decay varying as a function of wave frequency and sea-ice concentration (Eq. 3). Here, modeled spectral energy density $E(f)$ is compared to observed $E(f)$ and shipboard imagery (Fig. 5). For the observed $E(f)$, 95% confidence intervals were determined from the WAFO toolbox (dashed black, Fig. 5, and Collins III et al., 2015), while for the model $E(f)$ from a grid point closest to the ship position and neighboring points within a radius of 25 km were considered (dashed red and blue lines).

It has been previously established that during the blocking event (red region, Fig. 4), SWAN simulated wave height is over-estimated. The shipboard ice imagery indicates pack unbroken ice at this time (Fig. 5f), while the AMSR imagery suggests ice concentration in exceeding $a_{ice} = 0.90$ (Fig. 2a). The maximum observed $E(f)$ is at least two orders of magnitude smaller than those simulated without (blue) and with (red) wave-ice interaction (Fig. 5a). Five hours later on May 02, 21:30-22:30 after the breakup event (Fig. 5g, h), observed wave activity increases which is captured by the simulation with wave-ice interaction

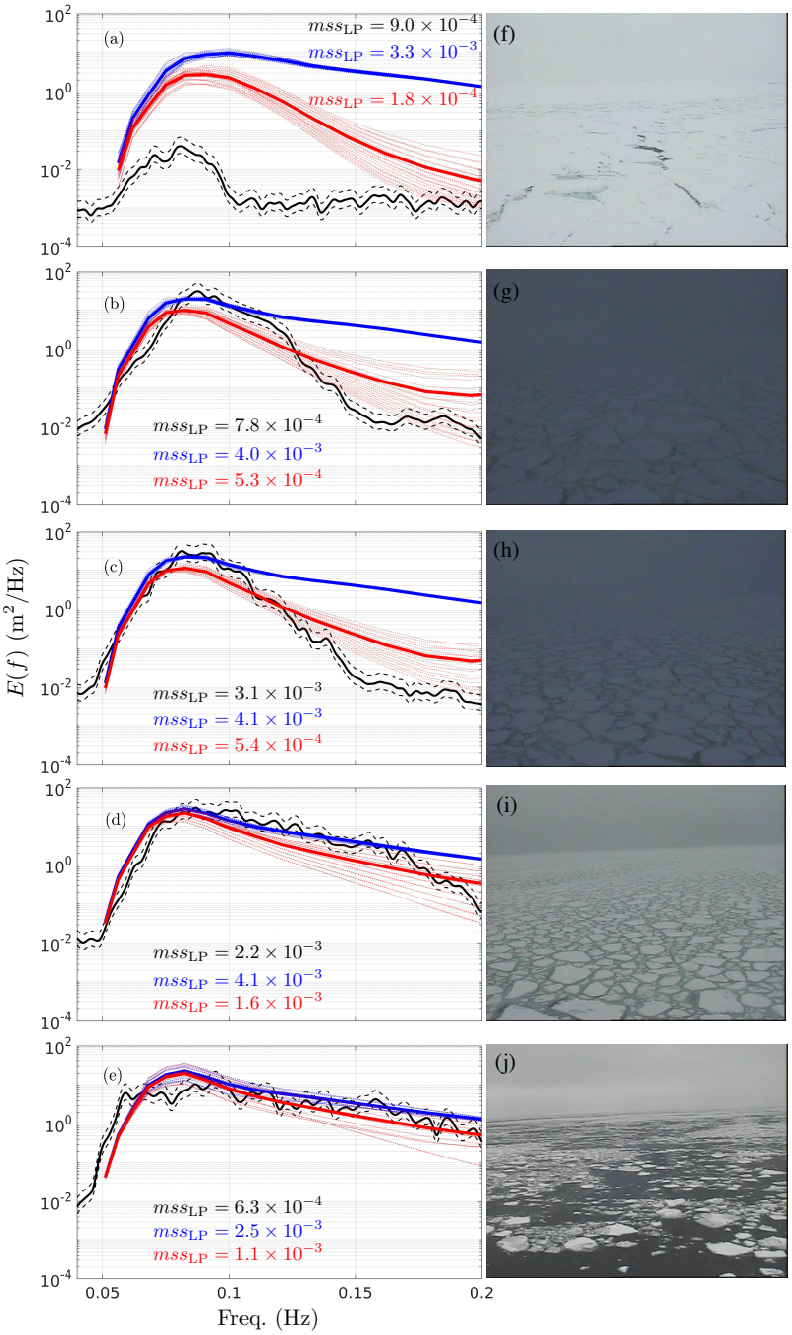

Figure 5: Observed (solid and dashed black) and modeled (blue w/o and red with sea-ice interaction) spectral energy density $E(f)$ versus frequency on (a) May 02, 2010, 16:30; (b) May 02, 2010, 21:30; (c) May 02, 2010, 22:30; (d) May 03, 2010, 02:30; and (e) May 03, 2010, 04:30. All times are in UTC. Shipboard camera imagery in (f-j) are for the times corresponding to those in (a-e). The dashed black lines are the 95% confidence intervals in observations, while the dashed red and blue lines are $E(f)$ estimates from a point within a radius of 25 km from the location closest to the observation location. The black, blue and red text in a-e are the modeled mean square slope (Eq. 9b) for observations, and simulations w/o and with wave-ice interaction.

(black and red, Fig. 5b,c). Also in this case, the decay in $E(f)$ at higher frequencies is well simulated as distinguished from the modeled $E(f)$ without and with wave-ice interaction (compare blue and red lines to black, Fig. 5b,c). Consequently the observed and modeled (R_I) mss_{LP} agree well (Fig. 4b).

As the storm intensifies and the vessel heads south through the MIZ (Fig. 5i,j) the observed wave activity is further enhanced and the role of sea-ice concentration is less evident (blue, red and black lines in Fig. 5d,e). This reduced role of sea-ice concentration is also expected as the vessel heads to the swell shadow (Fig. 3c,d), and $E(f)$ without and with wave-ice interaction are similar (Fig. 5e).

3.2. Gulf of Bothnia

The Gulf of Bothnia is located in the northernmost part of the Baltic Sea along the west coast of Finland (Fig. 6). This region experiences a seasonal ice cover every year from the month of January to April and is a good study site to explore wave-ice interaction (Tuomi et al., 2019). Furthermore, the needs for high resolution modeling with complex coastline features justifies usage of a regional wave model like SWAN. Previously, Tuomi et al. (2019) investigated the role of seasonal ice cover on the wave climate of the Baltic Sea using the WAM model along with treatment of wave-ice interaction as a function of ice concentration with no direct change in wave spectral evolution (*e.g.,* Tolman, 2003).

3.2.1. SWAN Model Setup

SWAN was set up without and with wave-ice interaction to simulate surface wave dynamics in the Gulf of Bothnia. The model grid with a mean resolution of $\Delta x = 1.75$ km and $\Delta y = 1.85$ km covers the entire Bothnian Sea and the Bothnian Bay, and a part of the Gulf of Finland (Fig. 6a). The model bathymetry is derived from ETOPO2 dataset (Center, 2006), and wind forcing every three hours is available from U.S. Navy's operational Coupled Ocean/Atmosphere Mesoscale Prediction System (COAMPS) at a resolution of 0.2°.

The Finnish Meteorological Institute (hereinafter FMI) provides daily ice concentration maps gridded at a resolution of $0.02° \times 0.01°$, for Longitude and Latitude, respectively, and available in a NETCDF format. This ice concentration map is updated daily by the FMI using a combination of in-situ measurements, satellite observations, and expertise in handling ice products in the study region (Tuomi et al., 2019).

SWAN simulations were setup with the same configuration as discussed for the Barents Sea test case. No wave boundary forcing was provided in the southern edge of the study domain (Fig. 6a). Simulations were conducted without (R_{NI}) and with (R_{I1}, R_{I2}) wave-ice interaction for a period of three months from January, 1-March, 31, 2018. For the simulations with wave-ice interaction, wave dissipation is considered for pancake ice with diameter 0.20-1 m (*i.e.,* $C_2 = 0.284 \times 10^{-3}$ and $C_4 = 1.53 \times 10^{-2}$, R_{I1}) and for broken ice floes with diameter 10-25 m (*i.e.,* $C_2 = 1.06 \times 10^{-3}$ and $C_4 = 2.30 \times 10^{-2}$, R_{I2}). Most of the comparison is done between R_{NI} and R_{I1}. Wind-input is scaled with the open water fraction ($\Omega_{iw} = 0$).

3.2.2. Ice Concentration

The seasonal sea-ice cover is a well-established feature in the Baltic Sea and usually extends for a period of 5-7 months, *i.e.,* from November to May. Yet, yearly variability in

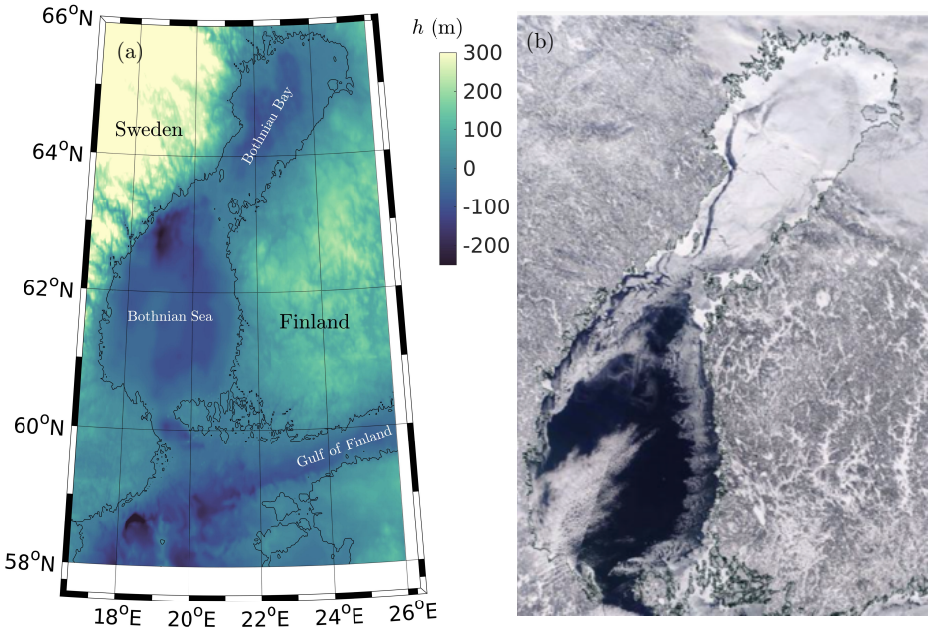

Figure 6: (a) SWAN grid for Gulf of Bothnia region with a mean grid resolution of $\Delta x = 1.75$ km and $\Delta y = 1.85$ km. Color shading is the bathymetry h. (b) Terra-MODIS visible band imagery showing water surface, ice and cloud cover in the Gulf of Bothnia on March 1, 2018.

ice season is large (Haapala and Leppäranta, 1996). For a mild winter, only the Bothnian Bay may be ice covered, while for a cold winter both Bothnian Bay and the Bothnian Sea maybe ice covered. Observations further suggest that the Bothnian Bay ice pack may be motionless even for extreme wind conditions (*i.e.,* $\geq$ 15 ms^{-1}, Haapala and Leppäranta, 1996). TERRA-MODIS visible band imagery (Fig. 6b) on March 1, 2018 indicates ice coverage in the northern part of Gulf of Bothnia and marginal ice or ice free region in the Bothnian Sea. Here, daily ice concentration from Jan. 1-March 31, 2018 is averaged to determine the monthly mean sea-ice concentration for the simulation period (Fig. 7).

In January, 2018, most of the study region in the Gulf of Bothnia is ice free (Fig. 7a). Yet, sea-ice is present in the strait between the Bothnian Bay and Bothnian Sea with $\langle a_{\text{ice}} \rangle > 0.25$ (21°E, 63°N, Fig. 7a), and in the shallow reaches of the Bothnian Bay with $\langle a_{\text{ice}} \rangle > 0.75$. Deeper waters of the Bothnian Bay are ice free in January, 2018. Later in the season, sea-ice is present throughout the Bothnian Bay with $\langle a_{\text{ice}} \rangle > 0.80$ (Fig. 7b). Even though a time variability of a_{ice} is not explicitly shown here (check supplementary material), most of Bothnian Bay except the northeastern tip is ice free till mid-January. However, by the first week of February, the entire bay is ice covered.

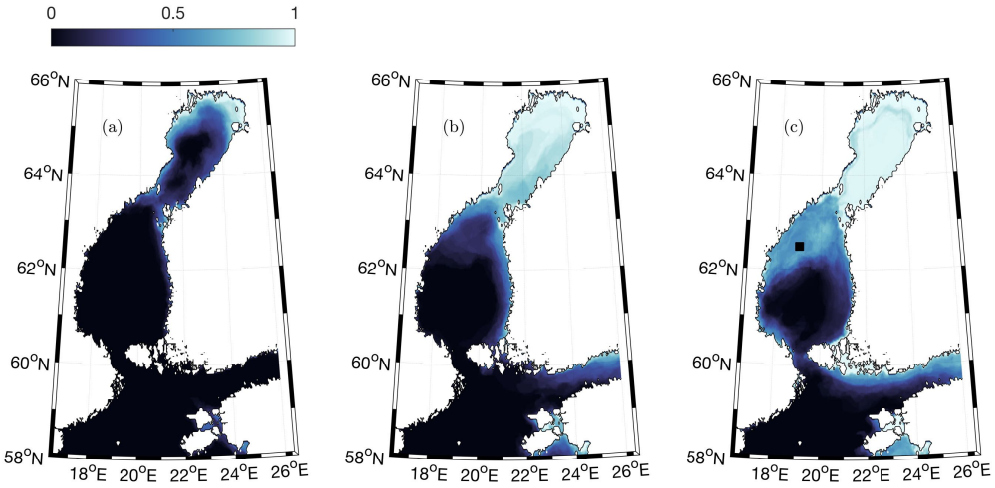

Figure 7: Area-averaged comparison of the mean ice concentration (color shading) in the Gulf of Bothnia from January (a), February (b) and March (c). This product is created using the daily ice concentration maps available from the FMI.

Ice concentration reduces further south and in February only shallow parts of the Bothnian Sea are ice covered (Fig. 7b). In the Gulf of Finland, sea-ice concentration $\langle a_{\text{ice}} \rangle$ is negligible in the south/southeastern flanges. The ice concentration increases to 0.5 in the northeastern edge of the Gulf of Finland (Fig. 7b). Ice growth does occur in the Bothnian Sea in late February with a_{ice} varying from 0-1 (Fig. 7c). For 2018, a_{ice} is high in late February and early March, and becomes more patchy in late March (not shown here). This region therefore is an interesting test bed for understanding wave-ice interaction in the MIZ.

3.2.3. Model Testing

Surface wave properties are measured in the Bothnian Bay and the Bothnian Sea by the FMI. However, the buoys are retrieved in the end of December for instrument protection and maintenance, to be redeployed in May (*personal communication, Antti Kangas, FMI*). Thus during the winter season no in-situ wave measurements are available. Significant wave height measured from satellite altimetry is however available for the study region (Ribal and Young, 2019). This dataset consists of altimetry based H_s from satellites JASON-2, JASON-3, CRYOSAT-2, HAI-YANG 2A, SENTINEL-3A and SARAL.

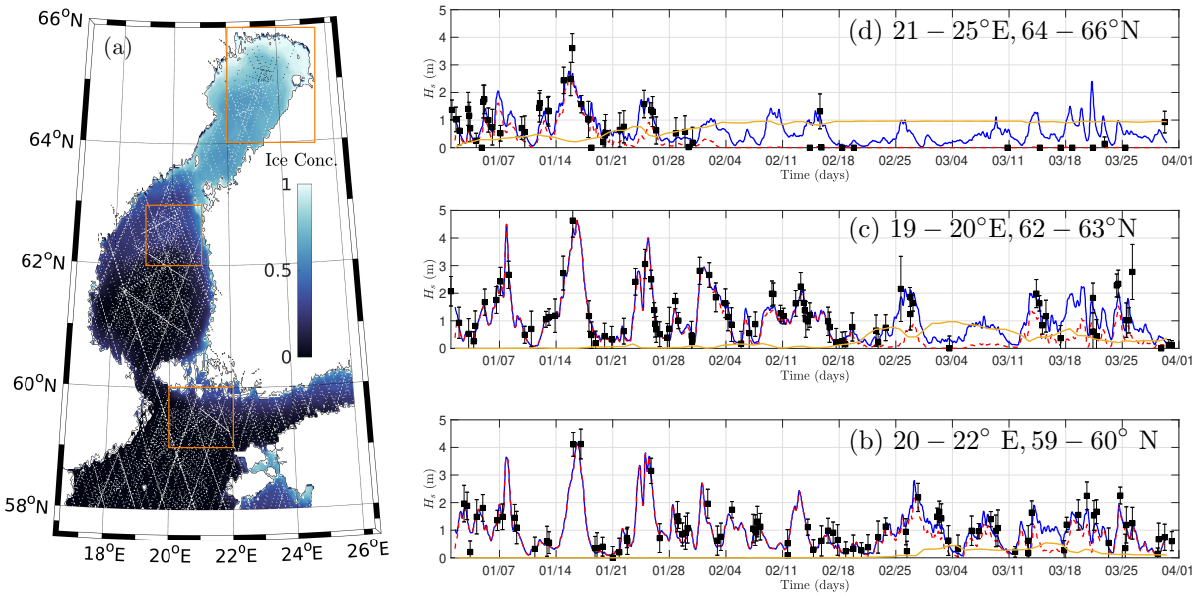

Figure 8: (a) Color shading showing the mean (Jan. -March, 2018) ice concentration in the Gulf of Bothnia along with locations (gray dots) corresponding to satellite altimeter measurements. Observed (black squares) and modeled significant wave height (blue and red) versus time (b, c, and d) corresponding to the orange rectangular regions in (a). Blue and red lines correspond to simulations w/o (R_{NI}) and with (R_{I1}) wave-ice interaction. The modeled significant wave height is averaged over the region denoted by the orange rectangle. The solid orange line in (b), (c) and (d) are averaged ice concentration.

Here, measurements from the first five satellites were obtained in the Gulf of Bothnia region for the simulation period. Measurements from SARAL had substantial errors and were discarded. Only quality controlled data (*i.e.,* QAQC flag=0, 1) in KU/KA band were considered for the analysis presented here. In addition to providing a mean H_s, every measurement also has a standard deviation determined from the 20 Hz KU/KA band altimeter (Ribal and Young, 2019). For standard deviation greater than 2.5 m, the data is flagged to be bad quality (*i.e.,* QAQC flag=4, Ribal and Young, 2019). In total approximately $7,500$ quality controlled data points were available for comparison to the model results (gray dots, Fig. 8a).

Satellite altimetry based measurement of H_s can be complicated in presence of sea-ice. Previous studies focused on H_s retrieval in regions with partial ice cover indicate that in

general H_s is higher for $a_{\text{ice}} \leq 0.3$, and sea-ice seems to affect altimetry measured H_s at concentration as low as $a_{\text{ice}} = 0.1$. It is not completely clear if this reduction in H_s is due to dissipation of waves in presence of ice, or if altimetry results are additionally impacted by presence of ice (Kudryavtseva and Soomere, 2016). Other studies using altimetry based H_s in the Baltic sea do not consider data collected for partial ice coverage (*e.g.,* Tuomi et al., 2019). Here, this criteria is not used to remove any altimetry data, instead the only filter is the QAQC flag provided with the observations (Ribal and Young, 2019). Regardless, caution must be exercised in interpretation of these observations.

Observed and modeled H_s over the simulation period are compared in multiple sub-regions within the Baltic Sea and the Gulf of Bothnia (orange boxes, Fig. 8a). The modeled sea-ice concentration and wave height within the sub-region is averaged to generate an area-averaged a_{ice} and H_s (yellow line, Fig. 8b-d). Simulations without (R_{NI}, solid blue) and with (R_{I1}, dashed red) wave-ice interaction are compared to all observations (solid black, Fig. 8b-d) available in the sub-region. Since observations are sparse and only available infrequently, they are not averaged.

In the Baltic Sea region, area averaged sea-ice concentration is zero for the simulation period (Fig. 8b). Both simulations R_{NI} and R_{I1} have the same area-averaged H_s and compare well to observations. In the northern Bothnian Sea a_{ice} is usually ≥ 0.3 after mid-February, which leads to reduced H_s in simulation R_{I1} (Fig. 8c). It is worth mentioning that reduced open water fraction and off-ice winds may also reduce wave height at a location in the MIZ.

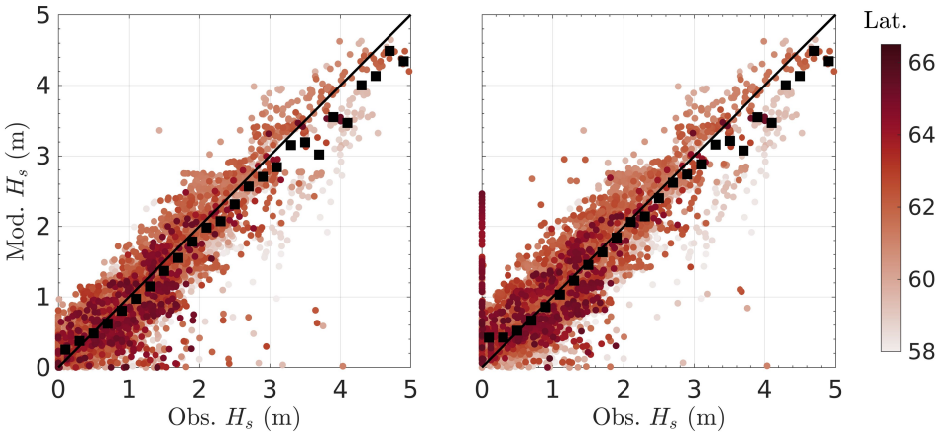

Figure 9: Obs. versus modeled H_s from simulation R_{I1} (a, with wave-ice interaction) and R_{NI} (b, w/o wave-ice interaction). Solid black squares are bin-averages and the solid black line is the 1:1 line. Model results were determined from the location closest to the observation location. Color indicates the latitude.

Strongest effect of sea-ice occurs in the Bothnian Bay with $a_{\text{ice}} > 0.9$, end of January onward (Fig. 8d). Modeled H_s from simulations R_{NI} and R_{I1} have similar magnitude in January and generally agree with observation. After January, H_s simulated by R_{I1} is basically zero, while as expected the simulation with R_{NI} has similar variability of H_s as modeled farther south (Fig. 8d). Even though observations in this region are even more sparse (Fig. 8a), there are at least multiple quality controlled observations which are also zero.

The area-averaged modeled H_s gives a general understanding of wave height variability in the sub-region. Yet, a more accurate way of comparing modeled H_s to observations is to determine it at a location closest to the observation location, as is considered in Fig. 9 for simulations with and without wave-ice interaction. It is clear that larger H_s is more common at lower latitudes, especially for the model simulation $\mathrm{R_{I1}}$ (Fig. 9a). Also, over-prediction of modeled H_s without wave-ice interaction at higher latitudes occurs where observations are mostly zero (Fig. 9b). Detailed error analysis of the best fit line between observations and the model results, by explicitly including the standard deviation associated with the observations, establishes that the simulation with wave-ice interaction is substantially better than those without (see Table. 1). Overall, the correlation coefficient $r^2(rmse)$ for $\mathrm{R_{I1}}$ and $\mathrm{R_{NI}}$ are 0.81(0.34 m) and 0.77(0.38 m). At higher latitudes ($\geq 63^\circ$ N), simulation $\mathrm{R_{I1}}$ has a correlation ($rmse$) of 0.69 (0.40 m), while for simulation $\mathrm{R_{NI}}$ 0.37 (0.63 m). Simulations with wave dissipation due to broken floes ($\mathrm{R_{I2}}$) has similar error statistics as for $\mathrm{R_{I1}}$.

Table 1: Results of linear regression of best fit line between observed (O) and modeled wave height (M), such that $M = aO + b$. Linear fitting includes uncertainty in both observations and model results. Standard deviation from satellite observations is the uncertainty in O, while modeled uncertainty is determined as the mean norm of the residual for a linear fit without any uncertainty in O or M. The uncertainty of fitted parameters (*i.e.,* a, b) are from a Monte Carlo simulation with 500 iterations, and by assuming errors are Gaussian and centered.

All Data Points	$\mathrm{R_{NI}}$	$\mathrm{R_{I1}}$
a	0.94 ± 0.01	0.98 ± 0.01
b	0.08 ± 0.01	-0.02 ± 0.01
r^2	0.77	0.81
$rmse$ (m)	0.39	0.36
High Lat. ($> 63^\circ$ N)		
a	0.67 ± 0.04	0.95 ± 0.03
b	0.49 ± 0.04	-0.01 ± 0.03
r^2	0.38	0.69
$rmse$ (m)	0.63	0.44

4. Discussion

4.1. Fetch-Scaling in the MIZ

Fetch available for wave generation is often a limiting parameter for wave growth in coastal regions and marginal seas (Hasselmann et al., 1973). For a given wind speed U_{10}, the corresponding fetch (X) and the associated wave energy ($E \propto H_s^2$) can be non-dimensionalized such that:

$$\mathcal{X} = \frac{gX}{U_{10}^2} \tag{10a}$$

and

$$\mathcal{E} = \frac{g^2 H_s^2}{16 U_{10}^4}. \tag{10b}$$

The relationship between $\mathcal{X}$ and $\mathcal{E}$ is such that,

$$\mathcal{E} = a\mathcal{X}^m, \tag{11}$$

where m is expected to vary from $0.75 - 1$ (Young, 1999). This simple fetch scaling law has been tested extensively in general (*e.g.,* Kahma and Calkoen, 1992; Young, 1999) and for the central Beaufort Sea (*e.g.,* Thomson and Rogers, 2014). Yet the appropriate fetch scalings for winds blowing over the MIZ is an open topic of research.

Recently, the relationship between fetch and wave energy in partial ice cover was studied over the western Arctic, with findings suggesting that the wave generation in the MIZ can be fetch limited for off-ice winds (Smith and Thomson, 2016), and the conventional fetch laws (*i.e.,* Eq. 11) can still be applied for off-ice winds with an "effective fetch" empirically scaled with the local ice concentration. The idea of wave generation in off-ice wind conditions has been further explored using TerraSAR-X imagery and local insitu wave measurements in the Beaufort Sea (Gemmrich et al., 2018). Particularly, an appealing idea of cumulative fetch is considered, where wave growth in the MIZ is considered to be a function of the ice coverage such that,

$$X = \alpha \sum X_i (1 - a_{\mathrm{ice}_i})^m, \tag{12}$$

where X_i is the downwind width of the region with sea-ice concentration of a_{ice_i}, α is the weighing parameter such that $0 \leq \alpha \leq 1$, and m is an empirical parameter. The value of α defaults to unity if local $a_{\mathrm{ice}_i} = 0$. Previously, $\alpha = 0.8$ and $m = 1$ have been found to agree well with observations in the Beaufort Sea (Gemmrich et al., 2018). Additional, fetch scaling laws for the MIZ have also been tested by assuming fetch origin at $a_{\mathrm{ice}} = 0.3$ or 0.5 (Gemmrich et al., 2018). Here, model simulated waves in the MIZ are used to diagnose the relative accuracy of multiple fetch scaling laws.

For the Gulf of Bothnia, the locations in the northern reaches of the Bothnian Sea are in the MIZ, especially in the latter half of the simulation period (*i.e.,* Feb 15 to March, 31, 2018). Here we consider a location at $19°\mathrm{E}, 62.5°\mathrm{N}$ (black dot, Fig. 7c) to test multiple fetch scalings. Particularly, two different fetch scaling are investigated for the simulation $\mathrm{R_{I1}}$ (*i.e.,* with wave-ice interaction and coefficients corresponding to pancake ice), (i) fetch scaling by assuming fetch origin at locations corresponding to $a_{\mathrm{ice}} \leq 0.3$; and (ii) cumulative fetch scaling (Eq. 12). For the cumulative fetch algorithm, only winds directed from $0 - 120°$ and $240 - 360°$ are considered as off-ice winds, and the algorithm reverts to a fetch scaling by assuming fetch origin same as in (i) for winds from other directions. Further, to limit incidents with weak and duration limited winds, all events with $U_{10} \leq 3.5$ ms^{-1} were not considered.

At the location of interest (black dot, $19°E$, $62.5°N$, Fig. 7c), $H_s = 0 - 5.65$ m is modeled for the simulation period with ice concentration varying from $a_{\mathrm{ice}} = 0 - 0.98$. The presence of higher concentration ice for a longer period of time leads to poor prediction of non-dimensional energy, $\mathcal{E}$ if fetch $\mathcal{X}$ is estimated using standard fetch laws with land boundaries as the fetch origin ($R^2 \leq 0.4$ and a best fit slope $m = 0.50$, not shown here). Note that the Pierson-Moskowitz limit for non-dimensional energy corresponding to pure

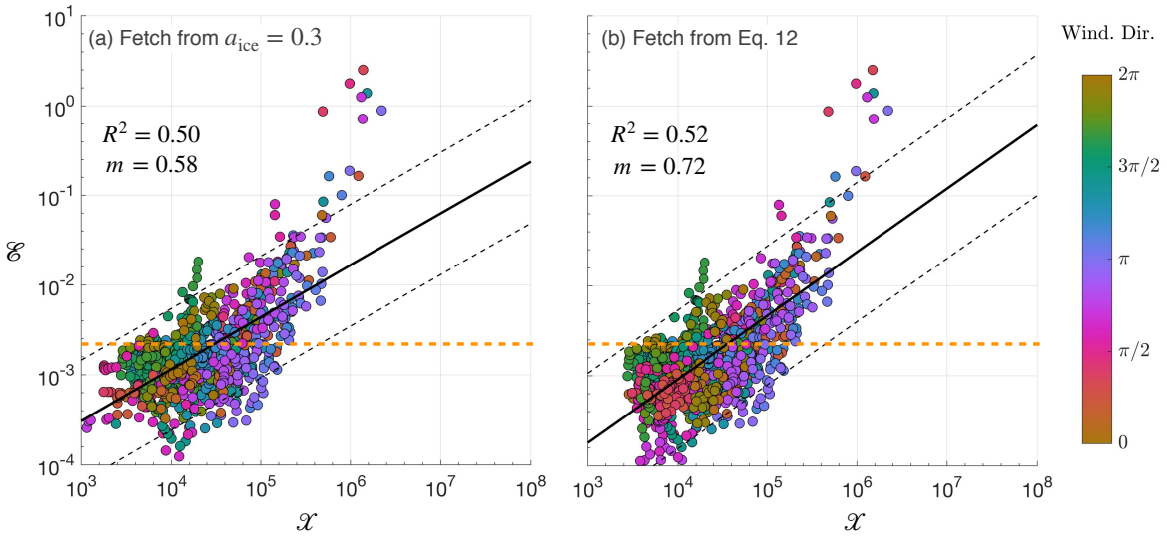

Figure 10: Non-dimensional fetch, $\mathcal{X}$ versus non-dimensional energy $\mathcal{E}$ for fetch estimates with origin corresponding to $a_{\text{ice}} = 0.3$ (a) and fetch estimates using the cumulative fetch algorithm (Eq. 12b) corresponding to a location 19°E, 62.5°N, shown in Fig. 7c. The solid black line is the best-fit line and the dashed black line are 95% confidence intervals. Colors represent the wind direction (meteorological convention) as a phase between $0 - 2\pi$. Orange dotted line is the non-dimensional energy limit for Pierson-Moskowitz spectrum.

wind seas is $\mathcal{E} = 3.64 \times 10^{-3}$, and modeled energy in the extreme upper right is not expected to fall on the best-fit line (Thomson and Rogers, 2014). For $\mathcal{X}$ estimates using $a_{\text{ice}} = 0.3$ as the fetch origin, $\mathcal{E}$ is correlated with $R^2 = 0.50, p < 0.05$ and the best fit slope is $m = 0.58$, *i.e.,* substantially less than the slope typically expected for wind-generated waves (Fig. 10a). Yet, this best fit line with 95% confidence intervals explains most of the modeled variability at this location. On the contrary with a cumulative fetch formulation, the best fit slope between $\mathcal{X}$ and $\mathcal{E}$ increases to $m = 0.72$, even though the correlation remains similar (*i.e.,* $R^2 = 0.52, p < 0.05$, Fig. 10b). Similar improvement in fetch scaling using a cumulative fetch estimate is identified at multiple other neighboring locations (not shown here).

4.2. Implications for Stokes Drift

Stokes drift represents the mass flux associated with surface waves. Near-surface Stokes drift is often comparable to circulation driven by other physical processes, and can modify tracer dispersal in coastal ocean and shallow seas. Moreover, the Stokes drift magnitude and Stokes drift shear are strongly dependent on the high frequency tail of the frequency spectrum. Since wave-ice interaction filters out high frequency signal through wave dissipation, it is expected that Stokes drift will be weaker and any upper-water column mixing will be inhibited in the MIZ. This change in Stokes drift and its shear has only received limited attention in the MIZ (*e.g.,* Smith and Thomson, 2016).

Near-surface Stokes drift magnitude $|\vec{u}^{\text{St}}|_{z=0}$ averaged for the month of March, 2018 is different for simulations with and without wave-ice interaction (Fig. 11a,b). For simulation R_{NI}, Stokes drift magnitude is up to 0.10 ms^{-1} in the Bothnian Sea and slightly smaller in

the Bothnian Bay. The general pattern of decrease in Stokes drift from south to north is evident for the simulation with wave-ice interaction R_{I1}, the magnitude is ≤ 0.05 ms^{-1} in the northern Bothnian Sea and ≤ 0.02 ms^{-1} in the Bothnian Bay. This general reduction in Stokes drift may have implications for pathways related to larval dispersal, transport and recruitment.

The spectral energy density $E(f)$ snapshot (March 13, 2018, 18:00:00) for simulations R_{NI}, R_{I1} and R_{I2} at location 19°E, 62.5°N is considered (black, blue and red lines, Fig. 11c). The $E(f)$ is diminished at almost all frequencies for simulations R_{I1} and R_{I2}. High frequency dissipation is stronger for the simulation assuming ice dissipation coefficients for broken floes (red, Fig. 11c). In absence of wave-ice interaction, the Stokes drift in the top 10 m of the water column is of the order $\mathcal{O}(10^{-2} - 10^{-1})$ ms^{-1}, decreasing by two orders of magnitude for simulations with coefficient of wave-dissipation corresponding to pancake ice and broken floes (blue and red, Fig. 11d). Subsequently, the Stokes drift shear,

$$\sqrt{\left(\frac{\partial u^{\mathrm{St}}}{\partial z}\right)^2 + \left(\frac{\partial v^{\mathrm{St}}}{\partial z}\right)^2} \tag{13}$$

is also weaker in presence of ice (Fig. 11e). Not only does the Stokes drift shear reduce, the shape of near-surface shear also changes. In simulation R_{NI} the shear rolls off rapidly near-surface due to the high frequency content of the frequency spectra. In absence of this high frequency tail, the reduction in shear is gradual. These near-surface changes in Stokes drift shear has potential implications for upper-water column mixing and gas transfer.

4.3. Role of Ice Thickness

The model development conducted for wave-ice interaction also allows for inputting the ice thickness h_{ice} (this is an undocumented feature in the SWAN manual). Even though no direct formulation exists for wave dissipation solely due to ice thickness, h_{ice} is a prognostic variable available from sea-ice models (*e.g.,* Community ICe CODE, CICE), and is also available from new, experimental satellite-derived products (*e.g.,* Soil Moisture and Ocean Salinity, SMOS). Sea-ice thickness may also a play a role in wave dissipation. For example, simulations conducted for the Barents Sea suggest that even if the ice concentration provided to the model is similar to satellite observations, the simulated wave height and spectral energy may still be over-estimated (Fig. 5a).

Previous studies have derived modified dispersion relationship by treating ice thickness layer as a suspension of solid particles in water with known viscosity (*e.g.,* Keller, 1998). These analytical solutions suggest changes in wave propagation speed and subsequent attenuation of wave energy. A more complicated approach suggests treatment of the ice-ocean system as a homogeneous viscoelastic fluid overlying an inviscid fluid (Wang and Shen, 2010), which is implemented as the IC3 approach in WW3 (Rogers and Orzech, 2013). Preliminary analysis on relating wave attenuation to pancake ice thickness have been tested in the Weddell Sea, suggesting a strong relationship between the attenuation coefficient as a function of the wave period and ice thickness (Doble et al., 2015). Viscous propagation models configured for grease and pancake ice have been used to simulate wave propagation,

with ice thickness as a fitting parameter for model calibration (De Santi et al., 2018). Also, considering relative success in expressing wave dissipation as an empirical function of a_{ice}, with dissipation coefficients determined from field experiments in different ice types, it is possible to determine representative ice thickness from existing dataset and ongoing experiments. Following the IC4M2 approach, empirical parameterizations for the decay rate $k_i(f)$ can be developed as function of ice thickness (Rogers, 2019). These approaches are yet to be developed and tested.

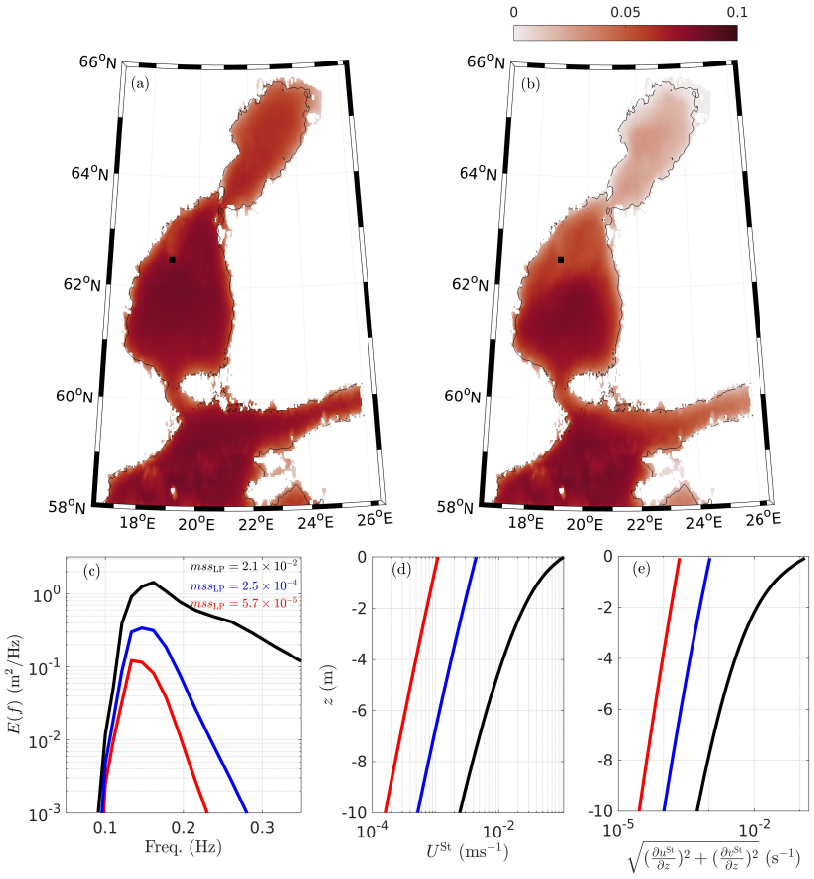

Figure 11: Mean (March, 2018) near-surface Stokes drift magnitude, $|\vec{u}^{\mathrm{St}}|$ over Gulf of Bothnia for simulation without (a, $\mathrm{R_{NI}}$) and with (b,$\mathrm{R_{I1}}$) wave-ice interaction. (c) Spectral energy density versus frequency; (d) Stokes-drift magnitude $|\vec{u}^{\mathrm{St}}|$ and (e) Stokes-drift shear $\sqrt{(\partial u^{\mathrm{St}}/\partial z)^2 + (\partial v^{\mathrm{St}}/\partial z)^2}$ versus vertical coordinates at location denoted by black square. Black, blue and red lines refer to simulations $\mathrm{R_{NI}}$, $\mathrm{R_{I1}}$ and $\mathrm{R_{I2}}$, respectively. Colored text in (c) is the estimated mean square slope (Eq. 9b).

5. Summary

Regional surface wave propagation model Simulating WAves Nearshore (SWAN) is developed to simulate wave-ice interaction including reduced wind-generated waves in the

presence of sea-ice, and wave dissipation. The wind generation process is modified by scaling the wind-generation source term with the open-water fraction, while wave dissipation process in presence of ice is simulated as an exponential wave energy decay as a function of ice concentration and wave frequency, as established from empirical fits to field measurements. This updated SWAN model is used to develop hindcasts for the Barents Sea and the Gulf of Bothnia.

Model simulations with wave-ice interaction generally capture the spectral energy density and dissipation at higher frequencies for the storm generated waves in the Barents Sea. Differences occur when the observed sea-ice is rigid, *i.e.,* SWAN, even with the correct ice concentration, produces energy variance much higher than those observed. In the shallow seas of Gulf of Bothnia, both wave generation and dissipation change in the presence of ice. Modeled significant wave height with wave-ice interaction compares reasonably well with satellite altimeter based estimates, and suggests a decreasing wave height trend from the Bothnian Sea to the Bothnian Bay, especially for late February and March, a trend also evident in the field observations. The modeled surface wave dynamics in the Gulf of Bothnia is further investigated to test modified fetch scaling laws for off-ice winds in the MIZ. The non-dimensional wave energy scales well with a non-dimensional fetch determined from a recently hypothesized cumulative fetch estimate as function of local ice concentration and empirical coefficients. In addition, one of the important findings from this work is the change in near-surface Stokes drift and Stokes drift shear in presence of sea-ice in the Gulf of Bothnia, which has consequences for Lagrangian transport and Langmuir turbulence. Finally recommendations for future model development in SWAN for including dependency of wave dissipation to ice thickness is considered. Future work will focus on application and validation of SWAN in the coastal Arctic, along with the possibilities for coupling between SWAN, regional ocean circulation model ROMS, and the sea-ice simulating model CICE.

6. Acknowledgments

This work was supported by the National Science Foundation, Office of Polar Programs (1818485), and the Office of Naval Research. Computational support was provided by the local HPC clusters maintained by Serhad Atakturk and Nick Burmeister. NK acknowledges the support from Antti Kangas, Finnish Meteorological Institute in providing sea-ice concentration. Development version of the SWAN code, observations, model results, plotting tools, and complete model simulations are available by contacting N. Kumar at nirni@uw.edu.

References

Agrawal, Y., Terray, E.A., Donelan, M.A., Hwang, P.A., III, A.J.W., Drennan, W.M., Kahma, K., Krtaigorodski, S.A., 1992. Enhanced dissipation of kinetic energy beneath surface waves. Nature 359, 219–220. doi:10.1038/359219a0.

Ardhuin, F., Boutin, G., Stopa, J., Girard-Ardhuin, F., Melsheimer, C., Thomson, J., Kohout, A., Doble, M., Wadhams, P., 2018. Wave attenuation through an Arctic marginal ice zone on 12 October 2015: 2. Numerical modeling of waves and associated ice breakup. Journal of Geophysical Research: Oceans 123, 5652–5668.

Ardhuin, F., Rogers, E., Babanin, A.V., Filipot, J.F., Magne, R., Roland, A., Van Der Westhuysen, A., Queffeulou, P., Lefevre, J.M., Aouf, L., et al., 2010. Semiempirical dissipation source functions for ocean waves. Part I: Definition, calibration, and validation. Journal of Physical Oceanography 40, 1917–1941.

Ardhuin, F., Sutherland, P., Doble, M., Wadhams, P., 2016. Ocean waves across the Arctic: attenuation due to dissipation dominates over scattering for periods longer than 19 s. Geophysical Research Letters .

Bateson, A.W., Feltham, D.L., Schröder, D., Hosekova, L., Ridley, J.K., Aksenov, Y., 2019. Impact of floe size distribution on seasonal fragmentation and melt of arctic sea ice. The Cryosphere Discuss., https://doi. org/10.5194/tc-2019-44, in review .

Booij, N., Ris, R., Holthuijsen, L.H., 1999. A third-generation wave model for coastal regions: 1. Model description and validation. Journal of Geophysical Research: Oceans 104, 7649–7666.

Boutin, G., Ardhuin, F., Dumont, D., Sévigny, C., Girard-Ardhuin, F., Accensi, M., 2018. Floe size effect on wave-ice interactions: Possible effects, implementation in wave model, and evaluation. Journal of Geophysical Research: Oceans 123, 4779–4805.

Bretherton, F.P., Garrett, C.J.R., 1968. Wavetrains in inhomogeneous moving media. Proceedings of the Royal Society of London. Series A. Mathematical and Physical Sciences 302, 529–554.

Center, N.G.D., 2006. 2-minute gridded global relief data (ETOPO2) v2.

Chen, D.D., Ruf, C.S., Gleason, S.T., 2016. Response time of mean square slope to wind forcing: An empirical investigation. Journal of Geophysical Research: Oceans 121, 2809–2823.

Collins, C.O., Rogers, W.E., 2017. A Source Term for Wave Attenuation by Sea Ice in WAVEWATCH III: IC4. Technical Report. Naval Research Laboratory Stennis Space Center United States.

Collins III, C., Blomquist, B., Persson, O., Lund, B., Rogers, W., Thomson, J., Wang, D., Smith, M., Doble, M., Wadhams, P., et al., 2017. Doppler correction of wave frequency spectra measured by underway vessels. Journal of Atmospheric and Oceanic Technology 34, 429–436.

Collins III, C.O., Rogers, W.E., Marchenko, A., Babanin, A.V., 2015. In situ measurements of an energetic wave event in the arctic marginal ice zone. Geophysical Research Letters 42, 1863–1870.

Dalrymple, R.A., MacMahan, J.H., Reniers, A.J., Nelko, V., 2011. Rip currents. Annual Review of Fluid Mechanics 43, 551–581.

D'Asaro, E.A., 2014. Turbulence in the upper-ocean mixed layer. Annual review of marine science 6, 101–115.

De Santi, F., De Carolis, G., Olla, P., Doble, M., Cheng, S., Shen, H.H., Wadhams, P., Thomson, J., 2018. On the ocean wave attenuation rate in grease-pancake ice, a comparison of viscous layer propagation models with field data. Journal of Geophysical Research: Oceans 123, 5933–5948.

Doble, M.J., Bidlot, J.R., 2013. Wave buoy measurements at the Antarctic sea ice edge compared with an enhanced ecmwf wam: Progress towards global waves-in-ice modelling. Ocean Modelling 70, 166–173.

Doble, M.J., De Carolis, G., Meylan, M.H., Bidlot, J.R., Wadhams, P., 2015. Relating wave attenuation to pancake ice thickness, using field measurements and model results. Geophysical Research Letters 42, 4473–4481.

Fox, C., Squire, V.A., 1994. On the oblique reflexion and transmission of ocean waves at shore fast sea ice. Philosophical Transactions of the Royal Society of London. Series A: Physical and Engineering Sciences 347, 185–218.

Gemmrich, J., Rogers, W.E., Thomson, J., Lehner, S., 2018. Wave evolution in off-ice wind conditions. Journal of Geophysical Research: Oceans 123, 5543–5556.

Haapala, J., Leppäranta, M., 1996. Simulating the baltic sea ice season with a coupled ice-ocean model. Tellus A 48, 622–643.

Hasselmann, K., Barnett, T., Bouws, E., Carlson, H., Cartwright, D., Enke, K., Ewing, J., Gienapp, H., Hasselmann, D., Kruseman, P., Meerburg, A., Mller, P., Olbers, D., Richter, K., Sell, W., Walden, H., 1973. Measurements of wind-wave growth and swell decay during the Joint North Sea Wave Project (JONSWAP). Erganzungsheft zur Deutschen Hydrographischen Zeitschrift Reihe A(8), 95.

Hogan, T.F., Rosmond, T.E., 1991. The description of the navy operational global atmospheric prediction system's spectral forecast model. Monthly Weather Review 119, 1786–1815.

Hoque, M.A., Perrie, W., Solomon, S.M., 2019. Application of SWAN model for storm generated wave

simulation in the Canadian Beaufort Sea. Journal of Ocean Engineering and Science .

Kahma, K.K., Calkoen, C.J., 1992. Reconciling discrepancies in the observed growth of wind-generated waves. Journal of Physical Oceanography 22, 1389–1405.

Keller, J.B., 1998. Gravity waves on ice-covered water. Journal of Geophysical Research: Oceans 103, 7663–7669.

Kohout, A., Meylan, M., 2008. An elastic plate model for wave attenuation and ice floe breaking in the marginal ice zone. Journal of Geophysical Research: Oceans 113.

Kohout, A., Williams, M., Dean, S., Meylan, M., 2014. Storm-induced sea-ice breakup and the implications for ice extent. Nature 509, 604–617.

Komen, G.J., Cavaleri, L., Donelan, M., Hasselmann, K., Hasselmann, S., Janssen, P., 1996. Dynamics and modelling of ocean waves. Dynamics and Modelling of Ocean Waves, by GJ Komen and L. Cavaleri and M. Donelan and K. Hasselmann and S. Hasselmann and PAEM Janssen, pp. 554. ISBN 0521577810. Cambridge, UK: Cambridge University Press, August 1996. , 554.

Kudryavtseva, N.A., Soomere, T., 2016. Validation of the multi-mission altimeter wave height data for the baltic sea region. Estonian Journal of Earth Sciences 65, 161–175.

Liu, A.K., Holt, B., Vachon, P.W., 1991. Wave propagation in the marginal ice zone: Model predictions and comparisons with buoy and synthetic aperture radar data. Journal of Geophysical Research: Oceans 96, 4605–4621.

Liu, A.K., Mollo-Christensen, E., 1988. Wave propagation in a solid ice pack. Journal of Physical Oceanography 18, 1702–1712.

Liu, A.K., Peng, C.Y., Weingartner, T.J., 1994. Ocean-ice interaction in the marginal ice zone using synthetic aperture radar imagery. Journal of Geophysical Research: Oceans 99, 22391–22400.

Mei, C.C., 1989. The applied dynamics of ocean surface waves. volume 1. World scientific.

Melville, W.K., 1996. The role of surface-wave breaking in air-sea interaction. Annu. Rev. Fluid Mech. 28, 279–321.

Meylan, M.H., Bennetts, L.G., Kohout, A.L., 2014. In situ measurements and analysis of ocean waves in the Antarctic marginal ice zone. Geophysical Research Letters 41, 5046–5051.

Meylan, M.H., Masson, D., 2006. A linear boltzmann equation to model wave scattering in the marginal ice zone. Ocean Modelling 11, 417–427.

Mosig, J.E., Montiel, F., Squire, V.A., 2015. Comparison of viscoelastic-type models for ocean wave attenuation in ice-covered seas. Journal of Geophysical Research: Oceans 120, 6072–6090.

Newyear, K., Martin, S., 1999. Comparison of laboratory data with a viscous two-layer model of wave propagation in grease ice. Journal of Geophysical Research: Oceans 104, 7837–7840.

Phillips, O.M., 1985. Spectral and statistical properties of the equilibrium range in wind-generated gravity waves. J. Fluid Mech. 156, 495–531.

Ribal, A., Young, I.R., 2019. 33 years of globally calibrated wave height and wind speed data based on altimeter observations. Scientific data 6, 77.

Ris, R., Holthuijsen, L., Booij, N., 1999. A third-generation wave model for coastal regions: 2. verification. Journal of Geophysical Research: Oceans 104, 7667–7681.

Roach, L.A., Horvat, C., Dean, S.M., Bitz, C.M., 2018. An emergent sea ice floe size distribution in a global coupled ocean-sea ice model. Journal of Geophysical Research: Oceans 123, 4322–4337.

Rogers, W., Orzech, M.D., 2013. Implementation and testing of ice and mud source functions in WAVEWATCH III. Memorandum Report NRL/MR/7320–13-9462. Naval Research Laboratory. URL: `http://www7320.nrlssc.navy.mil/pubs.php`.

Rogers, W.E., 2019. Implementation of Sea Ice in the Wave Model Swan. Technical Report. NAVAL RESEARCH LAB WASHINGTON DC WASHINGTON United States.

Rogers, W.E., Babanin, A.V., Wang, D.W., 2012. Observation-consistent input and whitecapping dissipation in a model for wind-generated surface waves: Description and simple calculations. Journal of Atmospheric and Oceanic Technology 29, 1329–1346.

Rogers, W.E., Kaihatu, J.M., Hsu, L., Jensen, R.E., Dykes, J.D., Holland, K.T., 2007. Forecasting and hindcasting waves with the SWAN model in the Southern California Bight. Coastal Engineering 54, 1–15.

Rogers, W.E., Meylan, M.H., Kohout, A.L., 2018. Frequencey Distribution of Dissipation of Energy of Ocean Waves by Sea Ice Using Data from Wave Array 3 of the ONR Sea State Field Experiment. Technical Report. NAVAL RESEARCH LAB WASHINGTON DC WASHINGTON United States.

Rogers, W.E., Thomson, J., Shen, H.H., Doble, M.J., Wadhams, P., Cheng, S., 2016. Dissipation of wind waves by pancake and frazil ice in the autumn Beaufort Sea. Journal of Geophysical Research: Oceans .

Roland, A., Ardhuin, F., 2014. On the developments of spectral wave models: numerics and parameterizations for the coastal ocean. Ocean Dynamics 64, 833–846.

Smith, M., Thomson, J., 2016. Scaling observations of surface waves in the Beaufort Sea. Elem Sci Anth 4. doi:10.12952/journal.elementa.000097.

Squire, V.A., 2007. Of ocean waves and sea ice revisited. Cold Regions Sci. Tech. 49, 110–133.

Squire, V.A., 2020. Ocean wave interactions with sea ice: A reappraisal. Annual Review of Fluid Mechanics 52.

Squire, V.A., Dugan, J.P., Wadhams, P., Rottier, P.J., Liu, A.K., 1995. Of ocean waves and sea ice. Annu. Rev. Fluid Mech. 27, 115–168.

Steele, M., Morison, J.H., Untersteiner, N., 1989. The partition of air-ice-ocean momentum exchange as a function of ice concentration, floe size, and draft. J. Geophys. Res. 94, 12739–12750.

Stopa, J.E., Ardhuin, F., Girard-Adrhuin, F., 2016. Wave-climate in the Arctic 1992-2014: seasonality, trends, and wave-ice influence. The Cryosphere doi:10.5194/tc-2016-37.

Tejada-Martinez, A., Grosch, C., 2007. Langmuir turbulence in shallow water. part 2. large-eddy simulation. Journal of Fluid Mechanics 576, 63–108.

Thomson, J., Ackley, S., Girard-Ardhuin, F., Ardhuin, F., Babanin, A., Boutin, G., Brozena, J., Cheng, S., Collins, C., Doble, M., et al., 2018. Overview of the Arctic sea state and boundary layer physics program. Journal of Geophysical Research: Oceans 123, 8674–8687.

Thomson, J., Fan, Y., Stammerjohn, S., Stopa, J., Rogers, W.E., Girard-Ardhuin, F., Ardhuin, F., Shen, H., Perrie, W., Shen, H., Ackley, S., Babanin, A., Liu, Q., Guest, P., Maksym, T., Wadhams, P., Fairall, C., Persson, O., Doble, M., Graber, H., Lund, B., Squire, V., Gemmrich, J., Lehner, S., Holt, B., Meylan, M., Brozena, J., Bidlot, J.R., 2016. Emerging trends in the sea state of the Beaufort and Chukchi seas. Ocean Modelling 105, 1 – 12. URL: http://www.sciencedirect.com/science/article/pii/S1463500316300622, doi:http://dx.doi.org/10.1016/j.ocemod.2016.02.009.

Thomson, J., Rogers, W.E., 2014. Swell and sea in the emerging Arctic Ocean. Geophysical Research Letters , n/a–n/aURL: http://dx.doi.org/10.1002/2014GL059983, doi:10.1002/2014GL059983.

Thomson, J., Talbert, J., de Klerk, A., Brown, A., Schwendeman, M., Goldsmith, J., Thomas, J., Olfe, C., Cameron, G., Meinig, C., 2015. Biofouling effects on the response of a wave measurement buoy in deep water. Journal of Atmospheric and Oceanic Technology 32, 1281–1286. URL: http://dx.doi.org/10.1175/JTECH-D-15-0029.1, doi:10.1175/JTECH-D-15-0029.1.

Toba, Y., 1973. Local balance in the air-sea boundary processes. III. on the spectrum of wind waves. J. Oceanogr. Soc. Japan. 29, 209–220.

Tolman, H.L., 2003. Treatment of unresolved islands and ice in wind wave models. Ocean Modeling 5, 219–231.

Tolman, H.L., The WAVEWATCH III ® Development Group, 2014. User manual and system documentation of WAVEWATCH III ® version 4.18. Tech. Note 316. NOAA/NWS/NCEP/MMAB. 282 pp. + Appendices.

Tuomi, L., Kanarik, H., Bjorkqvist, J.V., Marjamaa, R., Vainio, J., Hordoir, R., Höglund, A., Kahma, K.K., 2019. Impact of ice data quality and treatment on wave hindcast statistics in seasonally ice-covered seas. Frontiers in Earth Science 7.

Wadhams, P., Squire, V.A., Ewing, J., Pascal, R., 1986. The effect of the marginal ice zone on the directional wave spectrum of the ocean. Journal of physical oceanography 16, 358–376.

Wadhams, P., Squire, V.A., Goodman, D.J., Cowan, A.M., Moore, S.C., 1988. The attenuation rates of ocean waves in the marginal ice zone. J. Geophys. Res 93, 6799–6818.

Wang, R., Shen, H.H., 2010. Gravity waves propagating into an ice-covered ocean: A viscoelastic model. Journal of Geophysical Research: Oceans 115.

Weber, J.E., 1987. Wave attenuation and wave drift in the marginal ice zone. Journal of physical oceanography 17, 2351–2361.

Young, I., 1999. Wind Generated Ocean Waves. Elsevier Ocean Engineering Book Series, Elsevier, New York.

Zhang, Y., Chen, C., Beardsley, R.C., Perrie, W., Gao, G., Zhang, Y., Qi, J., Lin, H., 2020. Applications of an unstructured grid surface wave model (FVCOM-SWAVE) to the Arctic Ocean: The interaction between ocean waves and sea ice. Ocean Modelling 145. doi:https://doi.org/10.1016/j.ocemod.2019.101532.